

This is an Open Access document downloaded from ORCA, Cardiff University's institutional repository: <https://orca.cardiff.ac.uk/id/eprint/133558/>

This is the author's version of a work that was submitted to / accepted for publication.

Citation for final published version:

Thomas, Christian, Stephen, Sharon O. and Davies, Christopher 2020. Effects of partial slip on the local-global linear stability of the infinite rotating disk boundary layer. *Physics of Fluids* 32 (7) , 074105. 10.1063/5.0012976

Publishers page: <http://dx.doi.org/10.1063/5.0012976>

Please note:

Changes made as a result of publishing processes such as copy-editing, formatting and page numbers may not be reflected in this version. For the definitive version of this publication, please refer to the published source. You are advised to consult the publisher's version if you wish to cite this paper.

This version is being made available in accordance with publisher policies. See <http://orca.cf.ac.uk/policies.html> for usage policies. Copyright and moral rights for publications made available in ORCA are retained by the copyright holders.



Effects of partial slip on the local-global linear stability of the infinite rotating disc boundary layer

Christian Thomas,^{1, a)} Sharon O. Stephen,² and Christopher Davies³

¹⁾*Department of Mathematics and Statistics, Macquarie University, NSW 2109, Australia*

²⁾*School of Mathematics and Statistics, University of Sydney, Sydney, NSW 2006, Australia*

³⁾*School of Mathematics, Cardiff University, Cardiff, CF24 4AG, UK*

A numerical investigation is undertaken on the effect of small-scale surface roughness on the local absolute and global stability of the flow due to a rotating disc. Surface roughness is modeled via the imposition of the partial-slip wall boundary condition, with radial and concentric anisotropic roughnesses and isotropic roughness considered. The effect of the partial-slip parameters on the neutral characteristics for absolute instability is presented, while the azimuthal mode numbers required for global linear instability to occur are determined for the genuine inhomogeneous base flow. Predictions for the threshold values for the azimuthal mode numbers needed for globally unstable behavior are also computed by coupling solutions of the Ginzburg-Landau equation with the local linear stability properties obtained using the homogeneous flow approximation. These are found to be in excellent agreement with the exact values realised from the numerical simulations. In general, surface roughness is demonstrated to stabilise the absolute instability as well as the global linear instabilities.

^{a)}christian.thomas@mq.edu.au

I. INTRODUCTION

The effect of small-scale roughness on rotating boundary layer flows, as a means of delaying transition to turbulence, has been the focus of several recent numerical studies^{1–3}. In general, an increase in the critical Reynolds number for turbulent flow leads to drag reduction. Thus, this passive flow control strategy could lead to practical applications in the aero industry. The infinite rotating disc boundary layer is of interest to gain insight into the stability mechanisms in three-dimensional boundary layers.

Previous studies concerning roughness on the rotating disc have focused on local convective instabilities, including crossflow⁴ and the viscous Coriolis mode^{5,6}. The numerical study of Cooper *et al.*¹ modeled small-scale surface roughness by imposing partial-slip boundary conditions at the wall for the flow due to a rotating disc⁷. Both anisotropic and isotropic roughnesses are able to be accounted for in this way. For the rotating disc, anisotropic roughness corresponds to radial grooves or concentric grooves. The results of the local linear stability analysis for the crossflow instability revealed that, generally, roughness led to higher critical Reynolds numbers and hence had a stabilising effect on the flow. The exception was for viscous instability modes which were destabilised by concentric grooves. These initial studies have been extended to other rotating boundary layers². The asymptotic structure of the inviscid convective modes has been described by Stephen⁸. A further study by Garrett *et al.*³ investigated the effect of an alternative formulation for surface roughness, corresponding to concentric grooves (radially-anisotropic), for the linear stability of the flow due to a rotating disc⁹. Results were comparable with the case of partial-slip considered by Cooper *et al.*¹ for the inviscid crossflow modes, with differences found for the viscous instability modes. More recently, these studies have been extended to consider the effect of surface roughness on the non-Newtonian flow due to a rotating disc¹⁰. Here partial-slip boundary conditions appropriate for the non-Newtonian viscosity model were imposed with the results revealing a stabilisation of local convective instabilities for isotropic roughness and also for radial grooves (azimuthally anisotropic roughness). The effect of roughness on the rotating disc flow has also been the subject of experimental investigations¹¹, however the authors could not discern between the effects of the roughness and the confinement of the rotating disc.

Lingwood¹² was the first to consider absolute instability for the rotating disc flow. Poten-

tially more dangerous than convective instabilities, absolute instabilities have been the subject of many investigations of rotating flows to establish a link with the onset of transition to turbulence. Lingwood¹² showed that absolute instability first appears for Reynolds numbers near that associated with transition and suggested that the absolutely unstable mechanism was the final stage in the laminar-turbulent transition process. However, Lingwood's study neglected the radial dependence of the basic flow (equivalent to the parallel-flow approximation in a two-dimensional boundary layer). Subsequently, Davies and co-workers^{13,14} demonstrated that, for the genuine inhomogeneous flow due to an infinite rotating disc, linear disturbances were globally stable.

The first studies to investigate global linear instability in the infinite rotating disc boundary layer concentrated on azimuthal mode numbers, n , close to those values for the onset of absolute instability, n_a say, and globally unstable behaviour could not be found. However, the recent investigation of Thomas and Davies¹⁵ revealed that global linear instability does in fact exist for sufficiently large azimuthal mode numbers (larger than n_a) and is characterised by a faster than exponential temporal growth. The situation is illustrated in figure 1, detailing the regions of local and global linear stability in the (Re, n) space, where Re is the Reynolds number. Thomas and Davies¹⁵ also speculate that global linear instability exists for other related rotating flows. Their follow-up study¹⁶ confirms this for the rotating cone boundary layer.

The discovery by Thomas and Davies¹⁵ that the rotating disc flow is globally linearly unstable, now allows us to complete the picture of the effect of partial-slip conditions on the flow instabilities possible in rotating disc boundary layers. In this study, we investigate for the first time, the effect of a partial-slip wall boundary condition on the development of local absolute and global linear instabilities. To achieve this goal, we follow the approach of Thomas and Davies¹⁵ and utilise the velocity-vorticity formulation developed by Davies and Carpenter¹⁷. We will show that anisotropic surface roughness can be used to delay the onset of absolute instability to significantly larger Reynolds numbers. Furthermore, disturbance development to the inhomogeneous flow is numerically simulated and the azimuthal mode numbers needed for global linear instability to occur are predicted using the Ginzburg-Landau equation¹⁸.

The problem formulation is presented in Sec. II with the description of the base flow due to a rotating disc with small-scale surface roughness modeled using partial-slip wall boundary

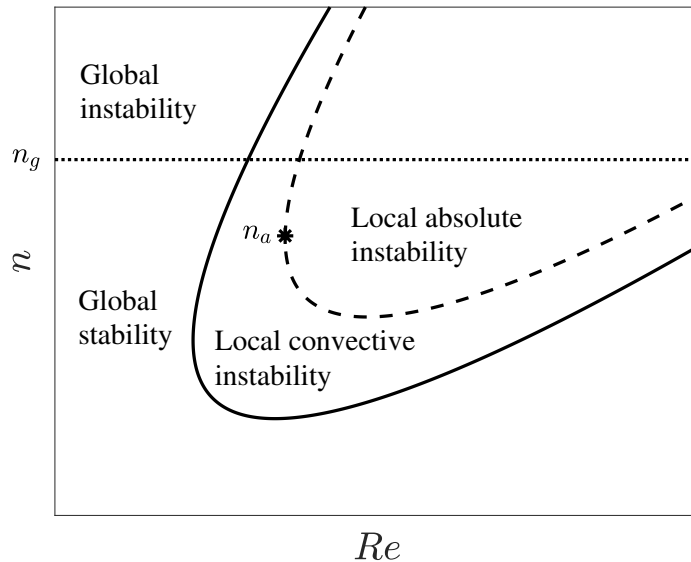


FIG. 1. Diagram illustrating the local and global linear stability of the rotating disc boundary layer (and family of flows), as determined by Thomas and Davies¹⁵.

conditions⁷. The linear perturbation equations are then presented for the velocity-vorticity formulation. Stationary crossflow disturbances are excited by periodic forcing with the homogeneous flow approximation. Critical Reynolds numbers and radial wavenumbers are computed, to compare with results of previous studies, which serve to validate the numerical code. Our results for local absolute instability, excited by impulsive wall forcing, are presented in Sec. III, with surface roughness shown to be stabilising. The description of how the Ginzburg-Landau equation is employed to predict the onset of global linearly unstable behavior follows in Sec. IV. Extensive numerical simulations reveal positive growth rates arise for $n > n_g$, where estimates for the threshold value n_g are found for different parameter values corresponding to the partial-slip conditions. The effect of radial inhomogeneity in the base flow is one focus of Sec. V. Additionally, we verify the accuracy of the predictions made in the previous section, for the azimuthal mode number n required for global linear instability to occur. Conclusions follow in Sec. VI.

II. FORMULATION

A. Base flow

A disc of infinite radius, rotates in an incompressible fluid of kinematic viscosity ν^* at a constant angular velocity Λ^* about the vertical axis that passes through the centre of the disc. Cylindrical polar coordinates are used to define the system, where r^* , θ and z^* denote the respective radial, azimuthal and axial directions. (Asterisks denote dimensional quantities.) Note that the coordinate system rotates with the disc.

The undisturbed steady flow field in this coordinate system is established using the von Kármán¹⁹ similarity variables

$$\mathbf{U}^* = \{r^*\Lambda^*F(z), r^*\Lambda^*G(z), \delta^*\Lambda^*H(z)\}, \quad (1)$$

where F , G and H represent the non-dimensional velocity profiles along the three coordinate directions. The parameter $\delta^* = \sqrt{\nu^*/\Lambda^*}$ denotes the constant boundary layer thickness used here to scale units of length; $r = r^*/\delta^*$ and $z = z^*/\delta^*$. On substituting (1) into the Navier–Stokes equation and the continuity equation in cylindrical coordinates, the following system of ordinary differential equations is derived

$$F'' = F'^2 + F'H - (G + 1)^2, \quad (2a)$$

$$G'' = 2F(G + 1) + G'H, \quad (2b)$$

$$0 = 2F + H', \quad (2c)$$

subject to the modified wall boundary conditions (to take account of the rough surface)

$$F = \lambda F'(0), \quad G = \eta G'(0), \quad H = 0 \quad \text{on} \quad z = 0, \quad (2d)$$

and freestream conditions

$$F \rightarrow 0 \quad \text{and} \quad G \rightarrow -1 \quad \text{as} \quad z \rightarrow \infty. \quad (2e)$$

A prime denotes differentiation with respect to z . The two parameters λ and η give measures of the roughness in the radial and azimuthal directions, respectively. Anisotropic roughness is established for $\eta > 0$ and $\lambda = 0$ (concentric grooves) and, $\eta = 0$ and $\lambda > 0$ (radial grooves),

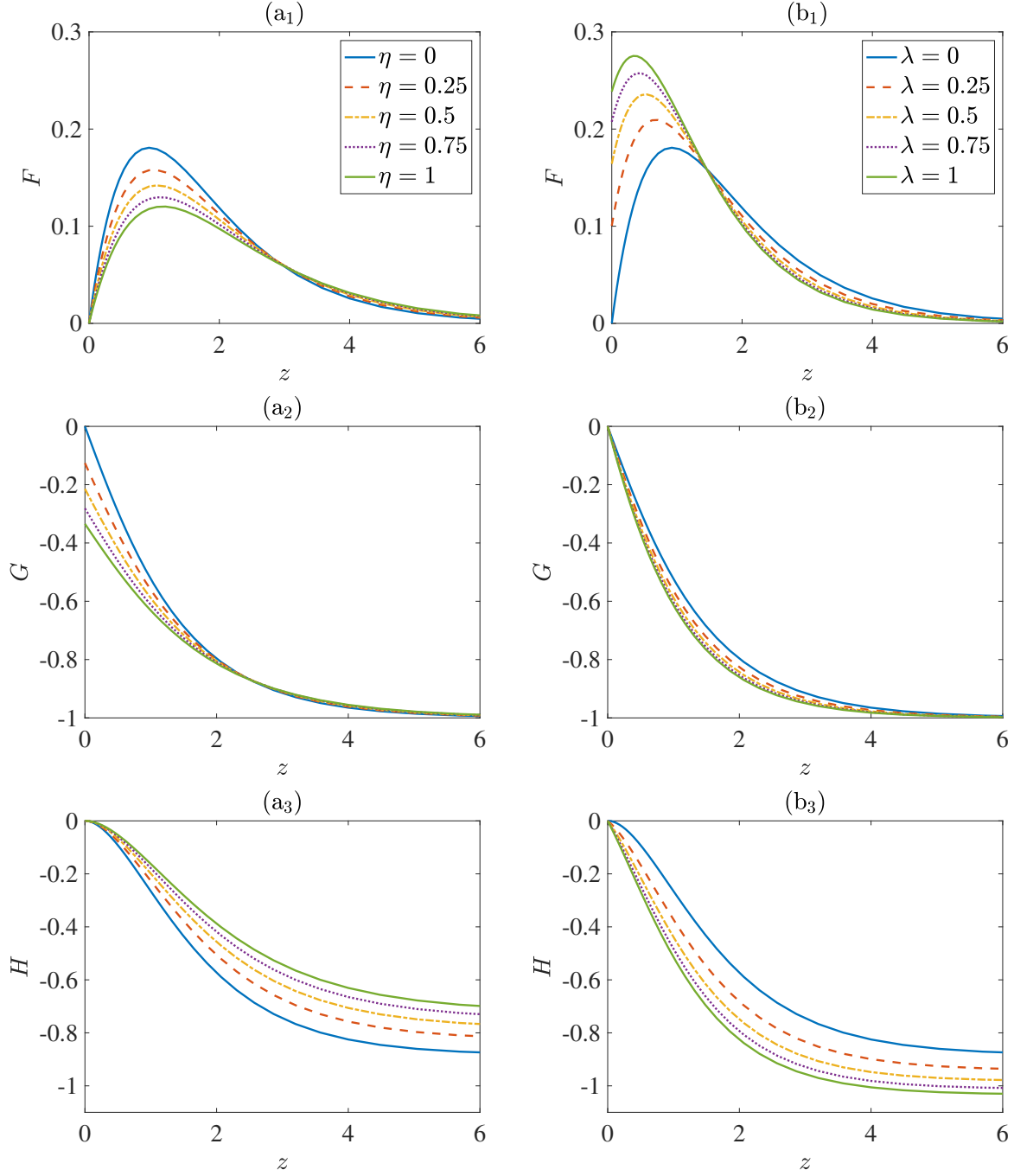


FIG. 2. Steady velocity flow profiles for (a_{*}) $\lambda = 0$ and variable η ; (b_{*}) $\eta = 0$ and variable λ . Subscripts 1, 2 and 3 match to the respective radial F , azimuthal G and wall-normal H velocity profiles.

while isotropic roughness corresponds to the case $\eta > 0$ and $\lambda > 0$. Figure 2 depicts velocity profiles F , G and H for different combinations of the parameters λ and η .

The non-dimensional base flow is then given as

$$\mathbf{U}_B(r, z) = \left\{ \frac{r}{Re} F(z), \frac{r}{Re} G(z), \frac{1}{Re} H(z) \right\}, \quad (3)$$

where the Reynolds number Re is defined as

$$Re = r_o^* \sqrt{\Lambda^* / \nu^*} \equiv r_o, \quad (4)$$

for some non-dimensional reference radius r_o .

B. Perturbation equations

Total velocity and vorticity fields are decomposed as

$$\mathbf{U} = \mathbf{U}_B + \mathbf{u}, \quad \boldsymbol{\Omega} = \boldsymbol{\Omega}_B + \boldsymbol{\omega},$$

where \mathbf{U}_B and $\boldsymbol{\Omega}_B = \nabla \wedge \mathbf{U}_B$ represent the undisturbed velocity and vorticity of the basic state (3), while the velocity and vorticity perturbation variables are defined as

$$\mathbf{u} = \{u_r, u_\theta, u_z\}, \quad \boldsymbol{\omega} = \{\omega_r, \omega_\theta, \omega_z\}.$$

Selecting the perturbation fields $\{\omega_r, \omega_\theta, u_z\}$ as the primary variables, the linearized disturbance evolution can be determined using the following set of governing equations

$$\frac{\partial \omega_r}{\partial t} + \frac{1}{r} \frac{\partial N_z}{\partial \theta} - \frac{\partial N_\theta}{\partial z} - \frac{2}{Re} \left(\omega_\theta + \frac{\partial u_z}{\partial r} \right) = \frac{1}{Re} \left(\left(\nabla^2 - \frac{1}{r^2} \right) \omega_r - \frac{2}{r^2} \frac{\partial \omega_\theta}{\partial \theta} \right), \quad (5a)$$

$$\frac{\partial \omega_\theta}{\partial t} + \frac{\partial N_r}{\partial z} - \frac{\partial N_z}{\partial r} + \frac{2}{Re} \left(\omega_r - \frac{1}{r} \frac{\partial u_z}{\partial \theta} \right) = \frac{1}{Re} \left(\left(\nabla^2 - \frac{1}{r^2} \right) \omega_\theta + \frac{2}{r^2} \frac{\partial \omega_r}{\partial \theta} \right), \quad (5b)$$

$$\nabla^2 u_z = \frac{1}{r} \left(\frac{\partial \omega_r}{\partial \theta} - \frac{\partial (r \omega_\theta)}{\partial r} \right), \quad (5c)$$

where

$$\nabla^2 = \frac{\partial^2}{\partial r^2} + \frac{1}{r} \frac{\partial}{\partial r} + \frac{1}{r^2} \frac{\partial^2}{\partial \theta^2} + \frac{\partial^2}{\partial z^2},$$

and

$$\mathbf{N} = \{N_r, N_\theta, N_z\} = \boldsymbol{\Omega}_B \times \mathbf{u} + \boldsymbol{\omega} \times \mathbf{U}_B.$$

The convective term \mathbf{N} depends on both the primary variables and the remaining perturbation components $\{u_r, u_\theta, \omega_z\}$. However, these so-called secondary variables can be explicitly

defined in terms of the primary variables, by rearranging the definition for vorticity and the solenoidal condition as

$$u_r = - \int_z^\infty \left(\omega_\theta + \frac{\partial u_z}{\partial r} \right) dz, \quad (6a)$$

$$u_\theta = \int_z^\infty \left(\omega_r - \frac{1}{r} \frac{\partial u_z}{\partial \theta} \right) dz, \quad (6b)$$

$$\omega_z = \frac{1}{r} \int_z^\infty \left(\frac{\partial(r\omega_r)}{\partial r} + \frac{\partial\omega_\theta}{\partial \theta} \right) dz. \quad (6c)$$

The linearization permits the no-slip conditions and the wall-normal zero-displacement conditions on the disc surface to be formulated as

$$u_r = -\frac{r}{Re} F'(0)\zeta, \quad u_\theta = -\frac{r}{Re} G'(0)\zeta, \quad u_z = \frac{\partial\zeta}{\partial t}, \quad (7a,b,c)$$

where ζ is a non-dimensional vertical wall-displacement that is used to excite disturbances in the boundary layer. For the subsequent investigation the wall-forcing ζ was centered about a radial location r_f and was either time-periodic or impulsive. The former forcing type was imposed with a fixed frequency, while the latter forcing type was prescribed for a finite time period that was sufficient to excite a broad range of disturbances. Substituting (7a) and (7b) into the definitions (6a) and (6b) for the secondary variables gives the following integral constraints for the primary variables ω_θ and ω_r :

$$\int_z^\infty \omega_\theta dz = \frac{r}{Re} F'(0)\zeta - \int_z^\infty \frac{\partial u_z}{\partial r} dz, \quad (8a)$$

$$\int_z^\infty \omega_r dz = -\frac{r}{Re} G'(0)\zeta + \int_z^\infty \frac{1}{r} \frac{\partial u_z}{\partial \theta} dz. \quad (8b)$$

Finally, the condition (7c) for u_z on the disc surface is unchanged, while all perturbations are assumed to asymptote towards zero in the far-field limit.

As we are only interested in the development of linear disturbances, it is possible to consider modes of the general form

$$\{\mathbf{u}, \boldsymbol{\omega}\} = \{\hat{\mathbf{u}}, \hat{\boldsymbol{\omega}}\} e^{in\theta}, \quad (9)$$

where $n = \beta Re$ is the integer valued azimuthal mode number. As a consequence of the circumferential periodicity of the disc, n can only take integer values. The azimuthal wavenumber β is more commonly employed in local stability studies¹, since β can be modeled as a continuous parameter.

C. Code validation

The accuracy of the base flow profiles and numerical scheme was first tested by drawing comparisons with the earlier study by Cooper *et al.*¹ who undertook a local linear stability study on the stationary crossflow instability. To achieve this, several disturbances were numerically simulated subject to a time-periodic wall-forcing with the frequency set to zero. Furthermore, the homogeneous flow approximation was implemented, whereby the radial dependence of the basic state (3) was ignored. This was achieved by setting the radius $r = Re$. For each combination of the roughness parameter set (λ, η) , two disturbances were simulated for flow settings (Re, n) near the conditions necessary for the onset of the stationary crossflow instability. The values for the integer-valued azimuthal mode number n and Reynolds number Re were carefully chosen using the results given in Cooper *et al.*¹. The method of bisection was then used to compute the critical conditions (Re_c, n_c) for stationary crossflow. Tables I and II compare the critical values for the onset of the stationary crossflow instability obtained by Cooper *et al.*¹ with those computed using the numerical simulations (given in bold). The critical wavenumber α_c was determined from the numerical simulations using the formula

$$\alpha_c = -\frac{i}{\omega_{\theta,w}} \frac{\partial \omega_{\theta,w}}{\partial r}, \quad (10)$$

where $\omega_{\theta,w}$ denotes the azimuthal vorticity perturbation on the disc surface. Excellent agreement was realised in all cases modeled with the minor variations attributed to the current analysis considering only integer-valued mode numbers n , while the earlier study by Cooper *et al.*¹ was based on the continuous azimuthal wavenumber β .

III. ABSOLUTE INSTABILITY

The numerical study was extended to model absolutely unstable disturbances. Base flow profiles were again based on the homogeneous flow approximation, while impulsive wall forcing was utilised to excite perturbations in the spatial-temporal plane. Many disturbances were simulated for an extensive range of roughness and flow parameters. Disturbance characteristics were computed and, neutral stability curves and critical conditions for absolute instability determined. In the subsequent discussion we will illustrate the process for computing critical parameter settings for the infinite rotating disc with concentric roughness

η	Re_c	n_c	α_c
0	286.1	22.2	0.384
0	285.9	22	0.371
0.25	312.3	18.3	0.366
0.25	313.5	18	0.351
0.5	336.8	16.1	0.358
0.5	338.1	16	0.345
0.75	358.9	14.4	0.342
0.75	361.3	14	0.320
1	379.1	13.2	0.331
1	381.3	13	0.316

TABLE I. Critical values for the onset of the stationary crossflow instability as found by Cooper *et al.*¹ for $\lambda = 0$ and $\eta \geq 0$ using a localised stability analysis with a homogeneous flow approximation. Values given in bold are determined from the numerical simulations using the same approximation.

λ	Re_c	n_c	α_c
0.25	380.1	37.0	0.353
0.25	379.6	37	0.346
0.5	527.5	59.4	0.318
0.5	525.8	59	0.311
0.75	722.6	89.4	0.286
0.75	719.4	89	0.282

TABLE II. Critical values for the onset of the stationary crossflow instability as found by Cooper *et al.*¹ for $\eta = 0$ and $\lambda > 0$ using a localised stability analysis with a homogeneous flow approximation. Values given in bold are determined from the numerical simulations using the same approximation.

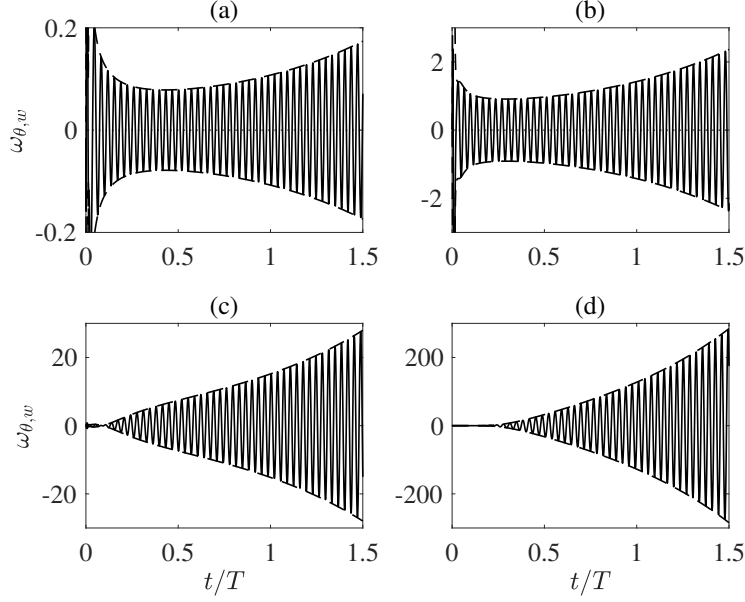


FIG. 3. Time histories for $\omega_{\theta,w}$ (solid lines), together with envelopes $\pm|\omega_{\theta,w}|$ (dashed), for an impulsively excited disturbance centered about $r_f = 600$ with $n = 70$ (and $Re = 600$). (a) $r = r_f - 25$; (b) $r = r_f$; (c) $r = r_f + 25$; (d) $r = r_f + 50$. The base flow is established using the homogeneous flow approximation for the roughness parameter settings $\eta = 0.5$ and $\lambda = 0$.

settings $\eta = 0.5$ and $\lambda = 0$.

Figure 3 displays time histories for a perturbation impulsively excited about the radial position $r_f = 600$ (and $Re = 600$) with the azimuthal mode number $n = 70$. Disturbance development is plotted as a function of time about the radial centre of forcing r_f along with three additional equally spaced radial locations: $r_f \pm 25$ and $r_f + 50$. The time variation is scaled on the disc rotation rate $T = 2\pi Re$. The azimuthal vorticity perturbation field at the wall $\omega_{\theta,w}$ is plotted (solid lines), along with the corresponding envelopes $\pm|\omega_{\theta,w}|$ (dashed) that are obtained from the complex-valued amplitude. In each instance plotted, including that upstream of the center of forcing, the perturbation grows as time increases. Hence, strong temporal growth is observed, which would indicate the disturbance is locally absolutely unstable.

The temporal frequencies and growth rates matching to the above disturbance are com-

puted using the formula

$$f = \frac{i}{\omega_{\theta,w}} \frac{\partial \omega_{\theta,w}}{\partial t}, \quad (11)$$

where the real and imaginary parts of f represent the temporal frequency and growth rate of the perturbation based on a local time non-dimensionalisation. The locally scaled frequency f is based on the ratio of the constant boundary-layer thickness and the circumferential speed of the rotating disc and is commonly used in local stability investigations such as that undertaken by Cooper *et al.*¹. However, in keeping with the earlier studies by Davies and co-workers^{13–15} we will present results based on a global time scaling that is defined by taking the inverse of the disc angular velocity. Thus, the globally defined frequency, $g = fRe$, will be presented. Figure 4(a,b) displays the globally defined frequency g_r and corresponding growth rate g_i associated with the four time histories plotted in figure 3. For all four curves plotted, the temporal frequency quickly converges towards a fixed value $g_r \approx -28.9$, while the matching growth rates are found to approach the value $g_i \approx 0.2$ for large time. Since the temporal growth rate is positive, the disturbance can be classified as being locally absolutely unstable.

The spatial-temporal disturbance development matching the above flow conditions is plotted in figure 4(c) using amplitude contours of the azimuthal vorticity at the wall $|\omega_{\theta,w}|$. Contours are drawn using a natural logarithmic scaling and have been normalised to have a maximum amplitude of unity at time $t = 0.2T$. The leading and trailing edges of the disturbance wavepacket are easily identified as the outer contours that originate from the radial centre r_f of the impulsive forcing. The leading edge propagates radially downstream (to the right) at a large constant velocity, while the trailing edge moves in the opposite radial direction (to the left) and is found to travel far more slowly. The illustration provides further confirmation that for the given flow settings, the disturbance is locally absolutely unstable as the leading and trailing edges propagate in opposite directions.

The above process was repeated for many combinations of the Reynolds number Re and azimuthal mode number n . Numerical simulations were carried out for azimuthal mode number step sizes $\Delta n = 1$ and 5. The smaller step size was employed in the parameter region where disturbances first become absolutely unstable, while the larger step size was utilised as the azimuthal mode number n was increased to larger values. For a fixed integer-valued n , numerical simulations were performed at step intervals of five Reynolds number units, with the method of bisection again utilised to determine the critical conditions for

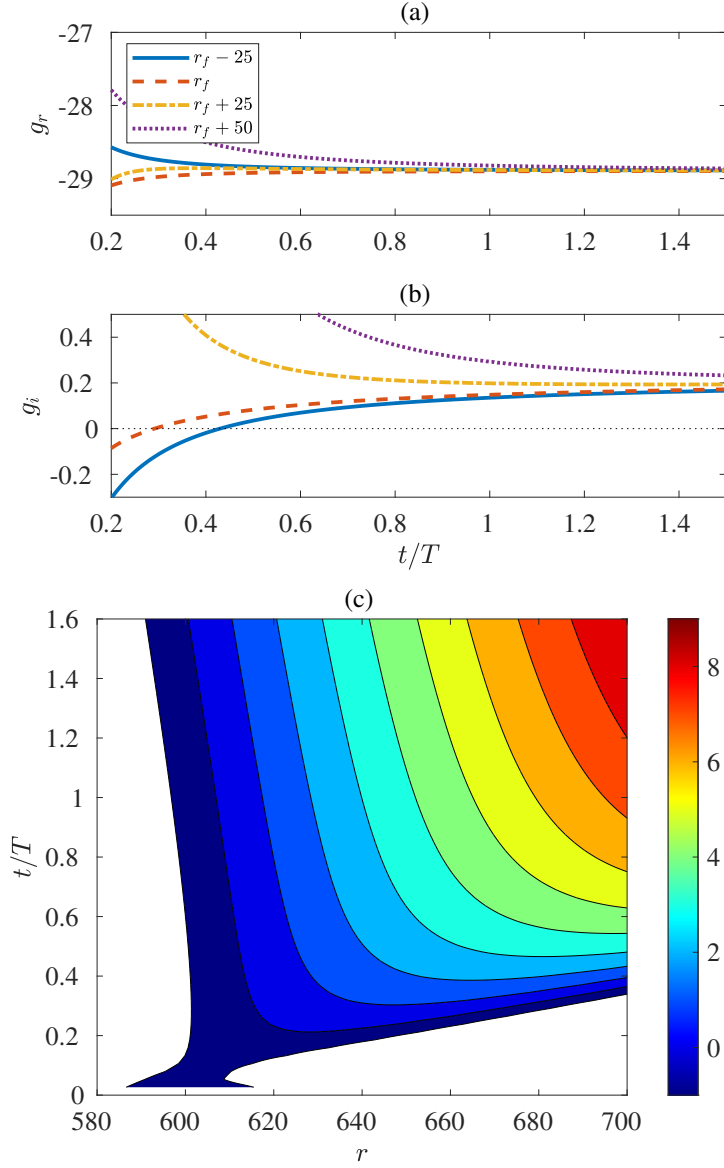


FIG. 4. (a) Temporal frequencies g_r ; (b) growth rates g_i ; (c) spatial-temporal development for the disturbance modeled in figure 3. (Contours in (c) are drawn using a logarithmic scaling.)

absolute instability; the Reynolds number Re where the temporal growth rate changes sign. The absolutely unstable neutral curve for the concentric roughness modeled above, with parameter settings $(\eta, \lambda) = (0.5, 0)$, is plotted in figure 5(a) using a chain line. The critical Reynolds number for local absolute instability $Re_a \approx 567$ is greater than that associated with the smooth rotating disc ($Re_a \approx 507$), while the critical azimuthal mode number $n_a = 68$ in

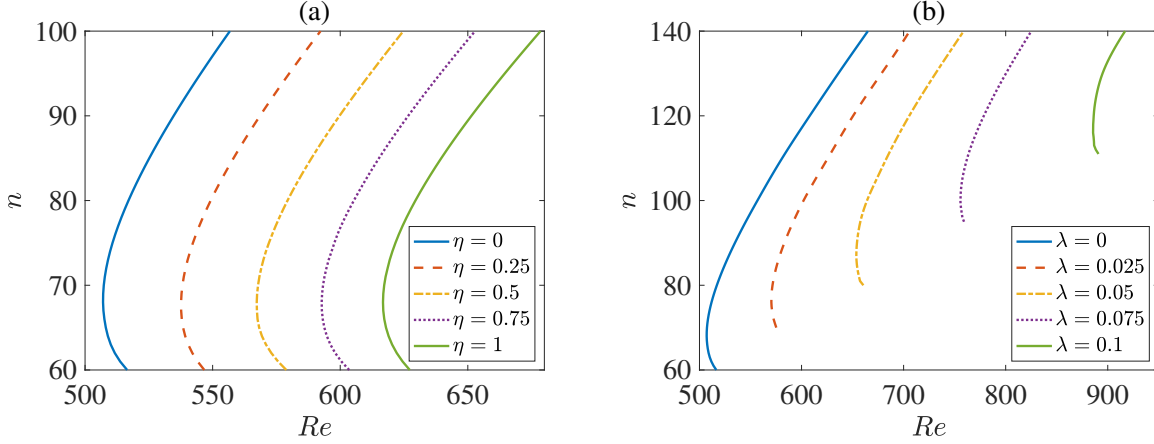


FIG. 5. Neutral stability curves for local absolute instability in the (Re, n) -plane. (a) $\lambda = 0$ and variable η ; (b) $\eta = 0$ and variable λ .

both cases.

The remaining line types plotted in figure 5 depict the absolutely unstable neutral curves for several concentric roughnesses ($\eta \neq 0$ and $\lambda = 0$) and radial roughnesses ($\lambda \neq 0$ and $\eta = 0$). Neutral stability curves are presented at $\Delta\eta = 0.25$ intervals for the concentric roughness models (those curves depicted on the left) and $\Delta\lambda = 0.025$ intervals for the radial roughness models (those curves depicted on the right). The critical Reynolds number Re_a increases as the degree of concentric and radial roughness increases. However, the radial roughness modeling approach establishes a considerably greater stabilising effect than the concentric roughness strategy. For the latter roughness type, the onset of absolute instability is raised to $Re_a \approx 617$ when $\eta = 1$, while for the former roughness strategy setting $\lambda = 0.1$ increases the critical Reynolds number to $Re_a \approx 886$. Hence, a significant stabilising effect is realised using the radial roughness approach for a relatively small roughness parameter setting.

The critical azimuthal mode number n_a for absolute instability is unchanged for those concentric roughness models investigated, with neutral stability curves shifted at regular intervals to the right. On the other hand, for the radial roughness modeling approach, the value for n_a increases with increasing λ . A complete listing of the critical parameters (including temporal frequencies $g_{r,a}$ and radial wavenumbers α_a) for local absolute instability

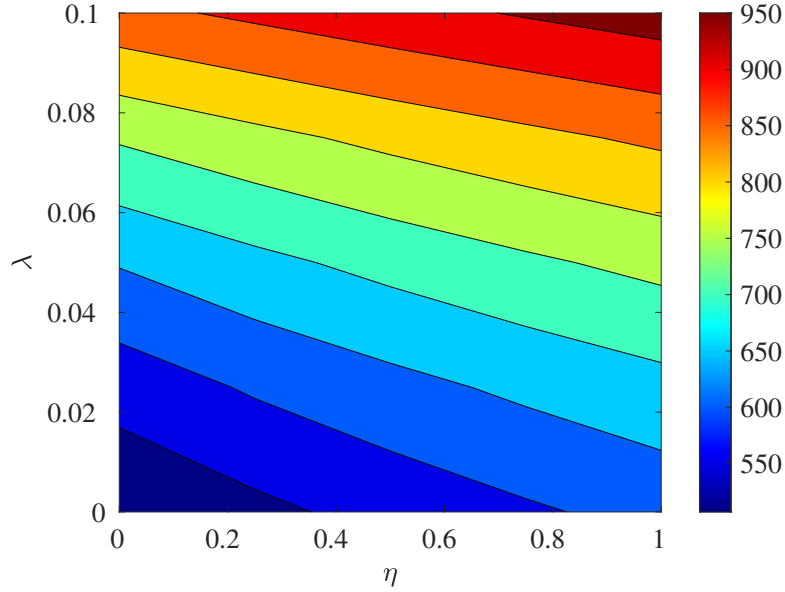


FIG. 6. Contour plot of the critical Reynolds number Re_a for local absolute instability in the (η, λ) -plane.

are tabulated in tables IV-VII in the appendix.

Figure 6 depicts contours of the critical Reynolds number for local absolute instability Re_a in the (η, λ) -plane. Blue contours in the lower left-hand corner display values $Re_a \approx 500$, while the red contours in the upper right-hand corner correspond to values $Re_a \approx 950$. Using the results plotted in figure 6 and presented in table IV it is observed that the critical Reynolds number Re_a increases almost linearly with the concentric roughness parameter η . Meanwhile, Re_a increases on a quadratic trend for the radial roughness parameter λ .

IV. PREDICTING THE ONSET OF GLOBALLY UNSTABLE BEHAVIOUR

Similar to the recent studies undertaken by Thomas and Davies^{15,16} we will now attempt to predict the azimuthal mode number n_g necessary for globally unstable behaviour to occur. To achieve this we will utilise the strategy developed by Thomas and Davies^{14,15,20} that is based on coupling the local stability computations with solutions of the linearised Ginzburg-Landau equation¹⁸. Disturbance characteristics from the numerical simulations undertaken

in the preceding section are carefully matched to the parameters of the Ginzburg-Landau equation that allow us to predict the critical value for n_g , such that for all $n > n_g$ a form of global linear instability emerges. Once we have made these predictions for the onset of global linear instability, we will verify our results by undertaking a numerical study of disturbance development to the genuine radially-dependent flow.

The linearised Ginzburg-Landau equation is given as

$$\frac{\partial A}{\partial t} + U \frac{\partial A}{\partial x} = \mu A + \gamma \frac{\partial^2 A}{\partial x^2}, \quad (12)$$

where $A(x, t)$ is a measure of the disturbance amplitude at the spatial location x and time t . The parameters μ , U and γ denote stability, convection and diffusion/dispersion effects, respectively. The stability parameter μ is allowed to vary linearly with the spatial direction. Thus,

$$\mu(x) = \mu_0 + \mu_1 x,$$

where the real and imaginary parts of μ_1 represent the respective spatial variations in the temporal growth rate and matching frequency. The Green's solution to (12) is then given as^{18,20}

$$G(x, t) = \sqrt{\frac{1}{4\pi\gamma t}} \exp\left(\frac{1}{2}\mu_1 x t + \frac{1}{12}\mu_1^2 \gamma t^3 - \frac{x^2}{4\gamma t}\right) \exp\{i(\alpha_0 x - f_0 t)\}, \quad (13a)$$

where

$$f_0 = i\left(\mu_0 - \frac{U^2}{4\gamma t}\right) \quad \text{and} \quad \alpha_0 = -i\frac{U}{2\gamma}, \quad (13b,c)$$

and complex parameters f_0 and $\alpha_0 = \alpha_{0,r} + i\alpha_{0,i}$ denote the temporal frequency and radial wavenumber, respectively. (Numerical values for both f_0 and α_0 are obtained from the numerical simulations of the rotating disc with the homogeneous flow approximation.) The spatial coordinate x has been shifted, so that the impulsive forcing is centered about $x = 0$. When the stability coefficient $\mu_1 = 0$ the imaginary part of μ_0 determines whether or not the flow is locally stable, convectively unstable or absolutely unstable.

The complex temporal frequency of the Green's solution (13a) is then determined using (11) (by replacing $\omega_{\theta,w}$ with G) with the growth rate given as

$$\text{Re}(f) \rightarrow \rho t^2 \quad \text{as} \quad t \rightarrow \infty \quad \text{for} \quad \rho = [(\mu_{1,r}^2 - \mu_{1,i}^2)\gamma_r - 2\mu_{1,r}\mu_{1,i}\gamma_i]. \quad (14a,b)$$

Thus, the form of the disturbance is governed by the stability coefficient $\mu_1 = \mu_{1,r} + i\mu_{1,i}$ and the diffusion/dispersion parameter $\gamma = \gamma_r + i\gamma_i$. Hence, if $\rho < 0$, the disturbance is classified as globally linearly stable, while if $\rho > 0$ the disturbance is globally linearly unstable.

Expressions for the stability coefficient μ_1 are formulated using the methods outlined in Thomas and Davies^{15,20} and given as

$$\mu_{1,r} = 2\frac{\partial g_i}{\partial x} \quad \text{and} \quad \mu_{1,i} = -2\frac{\partial g_r}{\partial x}, \quad (15a,b)$$

where $g = g_r + ig_i$ is the complex temporal frequency obtained via the numerical simulations of the disturbance development to the homogeneous flow. Similarly, the dispersion and diffusion effects $\gamma = \gamma_r + i\gamma_i$ are defined as

$$\frac{1}{\gamma} = \frac{\gamma_r}{|\gamma|^2} - i\frac{\gamma_i}{|\gamma|^2}, \quad (16a)$$

for

$$\frac{\gamma_r}{|\gamma|^2} = -\frac{2\alpha_{0,i}}{U} \quad \text{and} \quad \frac{\gamma_i}{|\gamma|^2} = \frac{2}{U} \left(\frac{\partial \phi}{\partial x} \Big|_{\max} - \alpha_{0,r} \right), \quad (16b,c)$$

where the convection velocity U is measured about the contour line that the disturbance achieves a maximum amplitude in the spatial-temporal plane and $\frac{\partial \phi}{\partial x} \Big|_{\max}$ represents a phase shift.

The analysis was applied to the concentric and radial roughnesses modeled in figure 5: $\lambda = 0$ and $\eta = 0, \dots, 1$ at step intervals $\Delta\eta = 0.25$ and, $\eta = 0$ and $\lambda = 0, \dots, 0.1$ at step intervals $\Delta\lambda = 0.025$. All quantities required to compute the growth rate ρ , given by (14), were carefully extracted from the numerical simulations for azimuthal mode numbers $n \in [60, 200]$. Results corresponding to the concentric roughness are plotted in figure 7(a), while figure 7(b) depicts the corresponding results matching to the radial roughness. In each instance, the growth rate ρ increases linearly with the azimuthal mode number n and in most cases a positive valued ρ is realised for sufficiently large n . There is a noticeable exception for the case $\eta = 0$ and $\lambda = 0.1$. For very large azimuthal mode numbers $n (> 200)$, numerical instabilities emerged that prevented disturbances being simulated for a sufficient time interval. Thus, stability characteristics required to compute ρ could not be determined. Nevertheless, given the trends of those other cases plotted in figure 7, it is expected that $\rho > 0$ will be attained for $n > 200$.

For the concentric roughness modelling approach, ρ is negative for the critical azimuthal mode number $n_a = 68$ for local absolute instability. However, $\rho > 0$ arises for $n_g > 83$ for all concentric roughnesses modeled. This would suggest that those inhomogeneous flows with concentric roughness will be globally linearly stable for smaller valued azimuthal mode numbers n and globally linearly unstable for larger valued n .

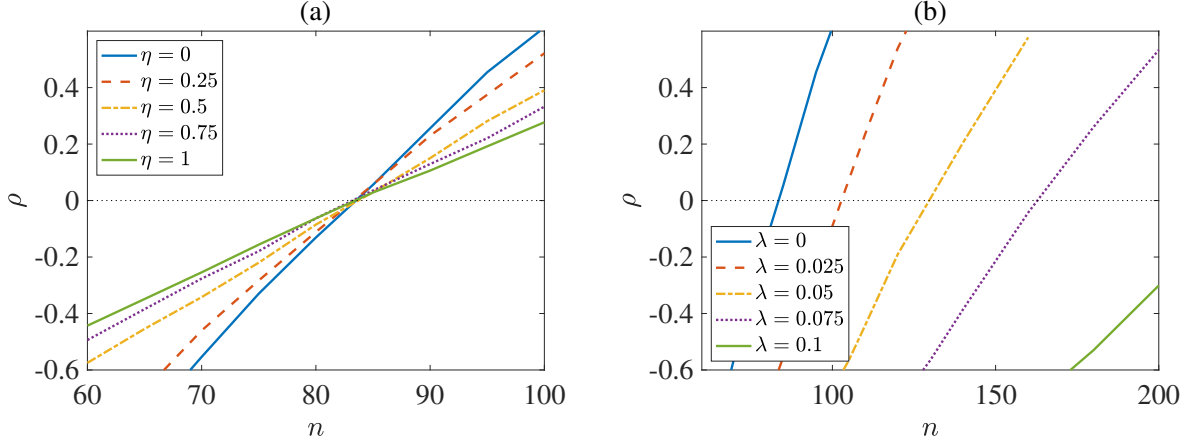


FIG. 7. Growth rates ρ as a function of the azimuthal mode number n for (a) $\lambda = 0$ and variable η ; (b) $\eta = 0$ and variable λ .

Growth rates ρ matching to the radial roughness suggest that disturbances will be globally linearly stable for the respective azimuthal mode numbers n_a and become globally linearly unstable for larger valued n . Table III compares the critical azimuthal mode numbers n_a for local absolute instability with the predicted values n_g for the appearance of globally linearly unstable disturbances. (Note that the predicted values based on coupling the Ginzburg-Landau equation with the numerical solutions of the homogeneous flow are labelled $n_{g,\text{pred}}$, while $n_{g,\text{in}}$ denotes the parameter range given by the numerical simulations of disturbances to the inhomogeneous flow.) In all instances modeled, the azimuthal mode number for global linear instability is considerably greater than that corresponding to the onset of local absolute instability. Furthermore, figure 7(b) and table III suggest that radial roughness establishes a significant stabilising effect and suppresses the appearance of globally linearly unstable characteristics to very large azimuthal mode numbers n .

V. DISTURBANCE DEVELOPMENT IN THE INHOMOGENEOUS FLOW

The numerical investigation was extended to the development of disturbances in the inhomogeneous flow, whereby the radial dependence of the base flow (3) was retained. The two major objectives in this section are to

λ	n_a	$n_{g,\text{pred}}$	$n_{g,\text{in}}$
0.0 (and $\eta \neq 0$)	68	83	80-90
0.025	76	103	100-120
0.05	87	129	120-140
0.075	100	163	160-180
0.10	116	200+	200+

TABLE III. Critical azimuthal mode numbers n_a for the appearance of local absolute instability and n_g for globally linearly unstable disturbances. Values $n_{g,\text{pred}}$ are predictions based on coupling solutions of the Ginzburg-Landau equation with the numerical solutions of the homogeneous flow, while $n_{g,\text{in}}$ represents the parameter range inferred by disturbance development to the inhomogeneous flow.

1. Ascertain the effect of radial inhomogeneity on the global linear stability characteristics of the rotating disc with surface roughness established via the partial-slip condition.
2. Verify the Ginzburg-Landau predictions, made in the previous section, for the azimuthal mode number n required for global linear instability to occur.

Figure 8 depicts the temporal frequencies, growth rates and spatial-temporal development for a disturbance impulsively excited about the radial position $r_f = 600$ with the azimuthal mode number $n = 70$ and the concentric roughness parameter settings $\eta = 0.5$ and $\lambda = 0$. (The equivalent results for the homogeneous flow are illustrated in figure 4.) There is a clear distinction between the homogeneous and inhomogeneous flow computations. Furthermore, the stability characteristics depicted in figure 8 are consistent with that found by Davies and co-workers^{13,15,20} for the rotating disc without roughness. Temporal frequencies g_r vary with the radial direction and in time; g_r increases over the time interval shown. Meanwhile, the corresponding temporal growth rates g_i decrease and are eventually negative at all radial positions plotted. Hence, the disturbance can be classified as being globally linearly stable. This is further demonstrated by the contour plot in figure 8(c) that illustrates the disturbance evolution in the spatial-temporal plane. The leading edge propagates radially outboard with a constant velocity comparable with that found for the homogeneous flow (recall figure 4(c)). However, the trailing edge acts in the opposite sense to that found

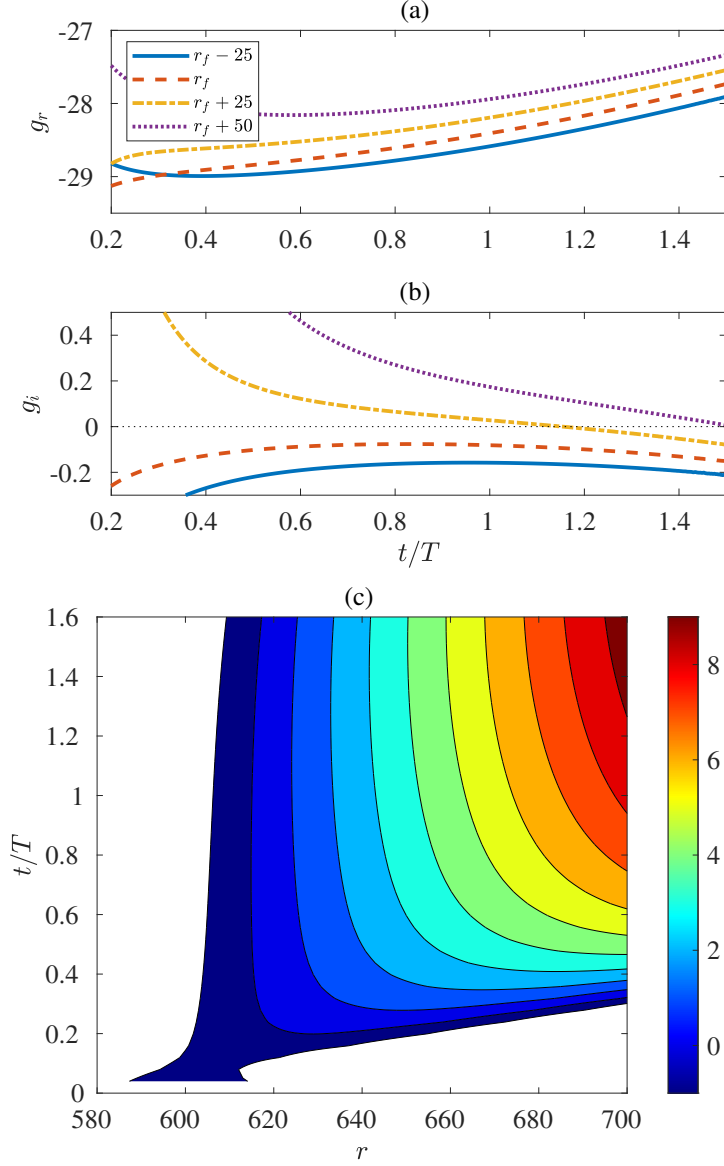


FIG. 8. (a) Temporal frequencies g_r ; (b) growth rates g_i ; (c) spatial-temporal development for a disturbance impulsively excited about $r_f = 600$ with $n = 70$ in the inhomogeneous flow. The roughness parameter settings $\eta = 0.5$ and $\lambda = 0$.

earlier (for the homogeneous flow) and propagates to the right with what appears to be an increasing velocity. Thus, the disturbance is globally linearly stable and dominated by convective stability characteristics.

Further disturbances were numerically simulated about $r_f = 625$ with the concentric

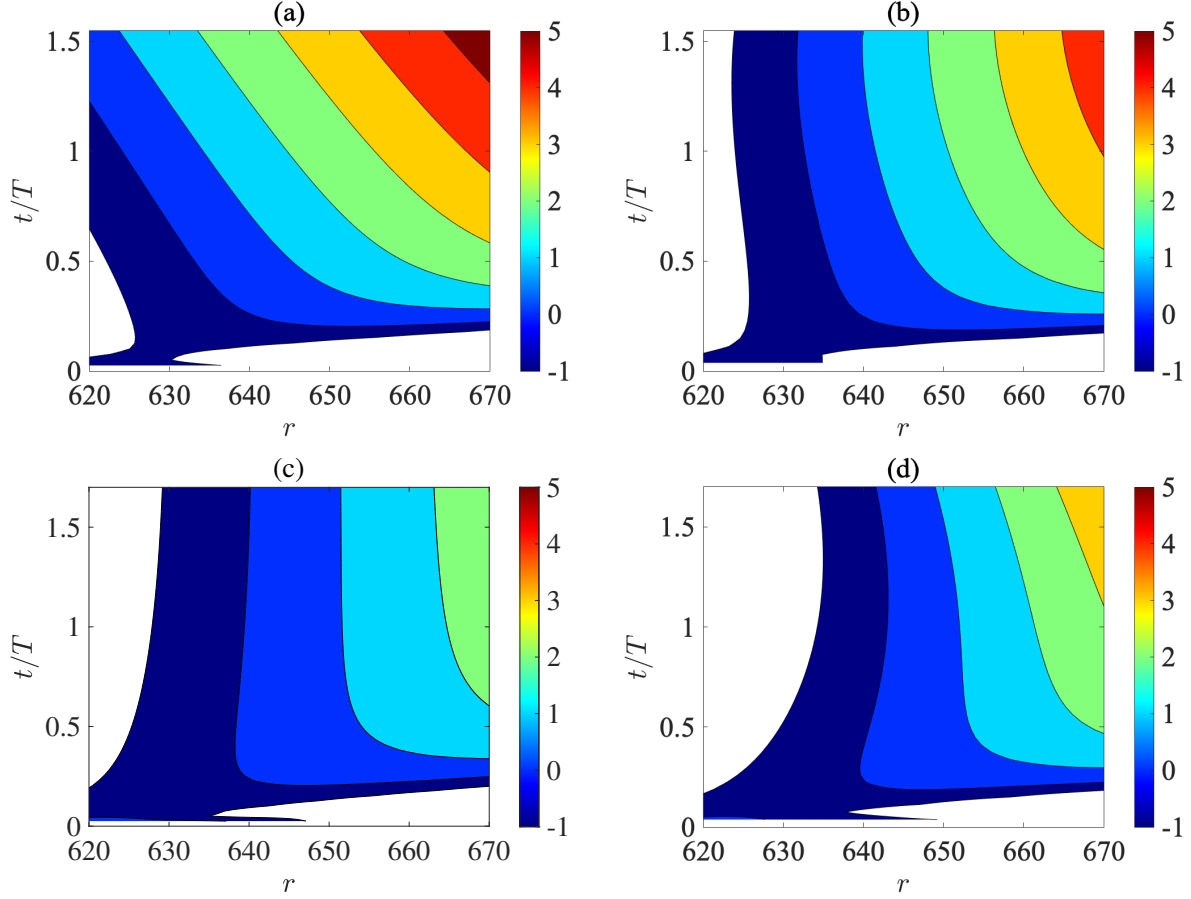


FIG. 9. Spatial-temporal development for impulsively excited disturbances centered about $r_f = 625$ (and $Re = 625$) with roughness parameter settings $(\eta, \lambda) = (0.5, 0)$ and (a, b) $n = 70$; (c, d) $n = 100$. Solutions on the left correspond to the homogeneous flow, while those on the right are associated with the inhomogeneous flow.

roughness parameter settings again given as $\eta = 0.5$ and $\lambda = 0$. Figure 9 depicts the disturbance wavepackets established for the azimuthal mode numbers $n = 70$ (figure 9(a, b)) and $n = 100$ (figure 9(c, d)). Illustrations on the left display results matching to the homogeneous flow (for $Re = 625$), while those on the right depict the equivalent solutions to the inhomogeneous flow. The two azimuthal mode numbers n were chosen to demonstrate any changes in the global linear stability characteristics as n is increased to larger values. The two contour plots corresponding to the homogeneous flow infer that the disturbance is strongly locally absolutely unstable for $n = 70$ and on the threshold of becoming locally

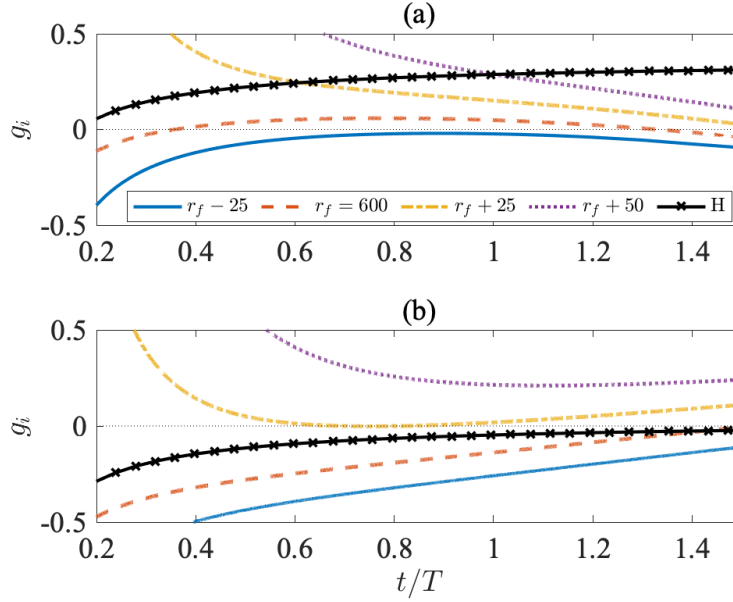


FIG. 10. Temporal growth rates associated with those disturbances illustrated in figure 9, for $r_f = 625$ and the roughness parameter settings $(\eta, \lambda) = (0.5, 0)$ and (a) $n = 70$; (b) $n = 100$. Solid-crossed lines labelled H depict the corresponding solutions in the homogeneous flow about the impulse centre.

absolutely unstable for $n = 100$. This behaviour is consistent with the neutral stability curve plotted in figure 5(a), where the critical Reynolds number for local absolute instability $Re_a \approx 568$ and 626 for the respective azimuthal mode numbers $n = 70$ and 100 .

Solutions matching to the inhomogeneous flow display very contrasting global linear stability features. For the smaller valued azimuthal mode number, $n = 70$, the trailing edge initially propagates radially upstream. However, about $t/T = 1.25$, the trailing edge can be seen to reverse direction and starts to propagate to the right and radially downstream. Thus, the disturbance displays convective characteristics and globally linearly stable behaviour prevails. Conversely, for the larger valued azimuthal mode number, $n = 100$, the trailing-edge initially propagates upstream, but after one rotation of the disc the trailing-edge changes direction and begins to propagate radially inward with an increasing velocity. This would suggest that strong temporal growth will eventually be realised and hence, a form of global linear instability will ensue.

Figure 10 depicts the temporal growth rates g_i associated with those disturbances described in figure 9(b, d). Temporal growth rates are again plotted about four equally spaced radially locations, while the equivalent homogeneous flow calculations are drawn using a solid-cross line. Results confirm that disturbances are globally linearly stable and unstable for $n = 70$ and $n = 100$, respectively. Growth rates decrease for the former case, while rapidly increasing growth rates are observed for the larger azimuthal mode number. Given the trends depicted in figure 10, negative and positive valued growth rates can be expected for the respective $n = 70$ and $n = 100$ cases, about all radial locations shown within a further half period of the disc rotation. Thus, there is a clear and marked difference between the two disturbances, which suggests that there is a critical azimuthal mode number $n_g \in [70, 100]$, for which $n > n_g$ globally linearly unstable behavior ensues.

In an attempt to improve the above numerical estimate for the emergence of globally linearly unstable disturbances, several perturbations were impulsively excited for azimuthal mode numbers $n \in [70 : 100]$ at intervals $n = 5$ about the radial location r_f that corresponds to the onset of absolute instability (based on those numerical simulations with the homogeneous flow approximation). Figure 11(a) depicts the temporal growth rates for the concentric roughness model $\eta = 0.5$ and $\lambda = 0$, with the values for the impulse centre r_f given in the figure legend. Growth rates are plotted in ascending order of n , with the lowest curve corresponding to $n = 70$ and the highest curve to $n = 100$. There is a noticeable change in behaviour as the azimuthal mode number n increases. For $n \leq 75$, temporal growth rates g_i are decreasing before the end of the time period shown. Hence, strong temporal decay and globally linearly stable behavior are realised for these particular disturbances. However, for larger valued azimuthal mode numbers, temporal growth rates increase over the entire time interval plotted. Thus, a form of global linear instability is observed that is characterised by a faster than exponential growth. The numerical calculations indicate that globally linearly unstable disturbances will first occur for azimuthal mode numbers $n_g \in [80, 90]$. Hence, for this particular roughness arrangement, numerical calculations are consistent with the Ginzburg-Landau analysis that predicted global linear instability would first arise for $n_g = 83$.

Temporal growth rates for a second concentric roughness and two radial roughnesses are plotted in figure 11(b-d); roughness parameters η and λ are as given in the caption. The three illustrations depict similar trends to that found for the roughness model $(\eta, \lambda) = (0.5, 0)$, with

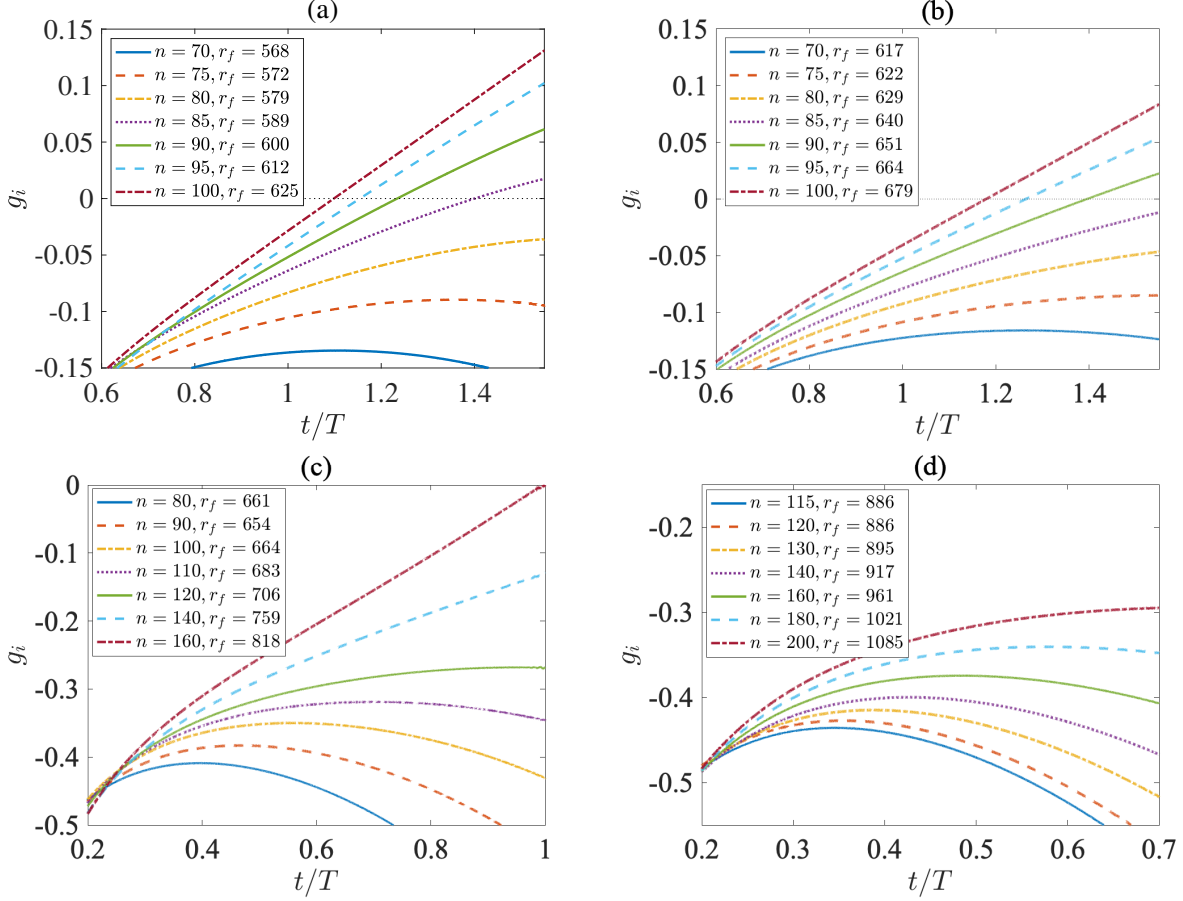


FIG. 11. Temporal growth rates g_i , for disturbances impulsively excited about the onset of absolute instability r_f for roughness parameter settings $(\eta, \lambda) =$ (a) $(0.5, 0)$; (b) $(1, 0)$; (c) $(0, 0.05)$; (d) $(0, 0.1)$.

growth rates increasing as the azimuthal mode number n increases. Results indicate that $n_g \in [80, 90]$ and $n_g \in [120, 140]$ for the two roughnesses $(\eta, \lambda) = (1, 0)$ and $(\eta, \lambda) = (0, 0.05)$, while calculations suggest that $n_g > 200$ is required for the radial roughness $(\eta, \lambda) = (0, 0.1)$. (As stated above, disturbance development for larger valued n was very difficult to simulate. Nonetheless, given the trends depicted in figure 11, positive and increasing growth rates may be expected for larger valued n .) Thus, the numerical computations are again in good agreement with the earlier Ginzburg-Landau predictions.

Longer time simulations, that may have been used to determine the exact azimuthal mode number n_g for the onset of globally unstable behavior, were very difficult to realise. As a

consequence of disturbances being linear, perturbations could grow exponentially without bound and thus achieve huge amplitudes that were impossible to model computationally. Nevertheless, our investigation indicates that the local-global linear stability of the rotating disc with partial-slip is similar to that found for the smooth rotating disc¹⁵. For sufficiently large azimuthal mode numbers n , a form of global linear instability emerges that is characterised by a stronger than exponential growth. For all cases modeled, the value for n was greater than that value associated with the onset of local absolute instability.

VI. CONCLUSIONS

A numerical investigation has been undertaken on the local and global linear stability of the infinite rotating disc boundary layer with roughness implemented via the partial-slip condition on the disc surface. Both anisotropic (including concentric and radial grooves) and isotropic roughnesses were modeled, while the evolution of disturbances was examined using the velocity-vorticity formulation developed by Davies and Carpenter¹⁷. Disturbance development was simulated for both the homogeneous and inhomogeneous flows, with the former established by fixing the radius.

The local linear stability study (based on the homogeneous flow) indicates that both concentric and radial roughnesses can be used to delay the onset of local absolute instability to Reynolds numbers greater than that associated with the rotating disc without roughness. Furthermore, the latter modeling approach was found to establish significantly greater control benefits than the former roughness strategy.

Numerical computations of the genuine inhomogeneous flow display global linear stability characteristics comparable with that found by Thomas and Davies^{15,16} for the infinite rotating disc and family of rotating cones. A form of global linear instability, characterised by a faster than exponential growth, arises when the azimuthal mode number n exceeds a threshold value n_g . For disturbances simulated at azimuthal mode numbers $n < n_g$, global linear stability prevails. In all instances modeled, it was found that $n_g > n_a$, where n_a denotes the critical azimuthal mode number for the onset of local absolute instability. Hence, the local-global linear stability of the infinite rotating disc with partial-slip can be described by the diagram depicted in figure 1. Additionally, the radial roughness strategy raised the azimuthal mode number n_g to considerably larger values than that corresponding to those

concentric roughnesses modeled.

Using the modeling developed by Thomas and Davies^{14–16,20} the azimuthal mode number n_g for the onset of globally unstable disturbances was predicted accurately by coupling solutions to the Ginzburg-Landau equation¹⁸ with local disturbance characteristics from the homogeneous flow simulations. For all cases modeled, predictions for n_g were consistent with the numerical simulations of the inhomogeneous flow. Thus, global linear stability characteristics can be estimated by the local linear stability analysis, without the need for undertaking a more thorough and computationally expensive study of the genuine radially dependent flow.

This initial study on the effect of surface roughness on absolute and global linear stability of flow due to a rotating disc could be extended to other rotating boundary layers. Of interest would be the effect of different roughness models, such as that considered by Garrett *et al.*³. It remains to be seen what the role of absolute or global instabilities play in the transition process for rotating flows with surface roughness and we eagerly await future experimental investigations of these flows.

DATA AVAILABILITY

The data that support the findings of this study are available from the corresponding author upon reasonable request.

REFERENCES

- ¹A. J. Cooper, J. H. Harris, S. J. Garrett, M. Özkan, and P. J. Thomas, “The effect of anisotropic and isotropic roughness on the convective stability of the rotating disk boundary layer.” *Phys. Fluids* **27**, 014107 (2015).
- ²B. Alveroglu, A. Segalini, and S. J. Garrett, “The effect of surface roughness on the convective instability of the bek family of boundary-layer flows,” *Eur. J. Mech. B/Fluids* **56**, 178–187 (2016).
- ³S. J. Garrett, A. J. Cooper, J. H. Harris, M. Özkan, A. Segalini, and P. J. Thomas, “On the stability of von kármán rotating-disk boundary layers with radial anisotropic surface roughness,” *Phys. Fluids* **28**, 014104 (2016).

- ⁴N. Gregory, J. T. Stuart, and W. S. Walker, “On the stability of three-dimensional boundary-layers with application to the flow due to a rotating disk,” *Philos. Trans. R. Soc. London, Ser A* **248**, 155–199 (1955).
- ⁵A. Faller and R. Kaylor, “A numerical study of the instability of the laminar ekman boundary-layer,” *J. Atmos. Sci.* **23**, 466–480 (1966).
- ⁶M. R. Malik, “The neutral curve for stationary disturbances in rotating-disk flow,” *J. Fluid Mech.* **164**, 275–287 (1986).
- ⁷M. Miklavčič and C. Y. Wang, “The flow due to a rough rotating disk,” *Z. Angew. Math. Phys.* **57**, 235–246 (2004).
- ⁸S. O. Stephen, “Effects of partial slip on viscous instabilities in rotating-disc boundary-layer flows,” AIAA paper AIAA-2017-4020 (2017).
- ⁹M. S. Yoon, J. M. Hyun, and J. S. Park, “Flow and heat transfer over a rotating disk with surface roughness,” *Int. J. Heat Fluid Flow* **28**, 262–267 (2007).
- ¹⁰A. A. Alqarni, B. Alveroğlu, P. T. Griffiths, and S. J. Garrett, “The instability of non-newtonian boundary-layer flows over rough rotating disks,” *J. Non-Newtonian Fluid Mech.* **273**, 104174 (2019).
- ¹¹M. Özkan, P. J. Thomas, A. J. Cooper, and S. J. Garrett, “Comparison of the effects of surface roughness and confinement on rotor-stator cavity flow,” *Engineering Applications of Computational Fluid Mechanics* **11**, 142–158 (2017).
- ¹²R. J. Lingwood, “Absolute instability of the boundary-layer on a rotating-disk,” *J. Fluid Mech.* **299**, 17–33 (1995).
- ¹³C. Davies and P. W. Carpenter, “Global behaviour corresponding to the absolute instability of the rotating-disc boundary layer,” *J. Fluid Mech.* **486**, 287–329 (2003).
- ¹⁴C. Davies, C. Thomas, and P. W. Carpenter, “Global stability of the rotating disc boundary layer,” *J. Eng. Math.* **57(3)**, 219–236 (2007).
- ¹⁵C. Thomas and C. Davies, “On the impulse response and global instability development of the infinite rotating-disc boundary layer,” *J. Fluid Mech.* **857**, 239–269 (2018).
- ¹⁶C. Thomas and C. Davies, “Global linear instability of rotating-cone boundary layers in a quiescent medium,” *Phys. Rev. Fluids* **4**, 239–269 (2019).
- ¹⁷C. Davies and P. W. Carpenter, “A novel velocity-vorticity formulation of the Navier-Stokes equations with applications to boundary layer disturbance evolution,” *J. Comp. Phys.* **172**, 119–165 (2001).

		λ				
		0	0.025	0.05	0.075	0.1
η	0	507.04	570.43	653.67	755.64	885.63
	0.25	537.63	606.18	687.02	786.02	910.43
	0.5	567.28	634.29	715.81	813.25	933.31
	0.75	592.73	660.55	741.53	837.38	954.53
	1	616.76	684.04	764.86	859.90	974.94

TABLE IV. Critical Reynolds number Re_a for the onset of absolute instability.

		λ				
		0	0.025	0.05	0.075	0.1
η	0	68	76	87	100	116
	0.25	68	76	86	99	114
	0.5	68	76	85	96	111
	0.75	68	75	84	94	106
	1	68	75	83	93	105

TABLE V. Critical azimuthal mode number n_a for the onset of absolute instability.

¹⁸R. E. Hunt and D. G. Crighton, “Instability of flows in spatially developing media,” Proc. R. Soc. London, Ser A **435**, 109–128 (1991).

¹⁹T. von Kármán, “Über laminare und turbulente reibung,” Z. Angew. Math. Mech. **1**, 233–252 (1921).

²⁰C. Thomas and C. Davies, “The effects of mass transfer on the global stability of the rotating-disk boundary layer,” J. Fluid Mech. **663**, 401–433 (2010).

Appendix A: Critical parameters for absolute instability

		λ				
		0	0.025	0.05	0.075	0.1
η	0	-17.478	-18.520	-20.115	-21.772	-23.480
	0.25	-23.974	-26.024	-28.707	-32.316	-36.134
	0.5	-28.397	-31.271	-34.304	-37.579	-43.476
	0.75	-31.782	-34.594	-38.227	-42.307	-47.024
	1	-34.438	-37.641	-41.185	-45.876	-51.203

TABLE VI. Critical frequency $g_{r,a}$ for the onset of absolute instability.

		λ				
		0	0.025	0.05	0.075	0.1
η	0	0.218-0.118 <i>i</i>	0.212-0.121 <i>i</i>	0.207-0.126 <i>i</i>	0.202-0.129 <i>i</i>	0.198-0.134 <i>i</i>
	0.25	0.204-0.110 <i>i</i>	0.199-0.112 <i>i</i>	0.194-0.117 <i>i</i>	0.192-0.119 <i>i</i>	0.186-0.123 <i>i</i>
	0.5	0.193-0.104 <i>i</i>	0.189-0.109 <i>i</i>	0.185-0.110 <i>i</i>	0.180-0.113 <i>i</i>	0.177-0.116 <i>i</i>
	0.75	0.185-0.100 <i>i</i>	0.186-0.107 <i>i</i>	0.177-0.105 <i>i</i>	0.173-0.108 <i>i</i>	0.169-0.111 <i>i</i>
	1	0.178-0.096 <i>i</i>	0.174-0.097 <i>i</i>	0.170-0.101 <i>i</i>	0.167-0.104 <i>i</i>	0.164-0.107 <i>i</i>

TABLE VII. Critical wavenumber α_a for the onset of absolute instability.